Influence of KCl and HCl on high temperature corrosion of HVAF-sprayed NiCrAlY and NiCrMo coatings

Esmaeil Sadeghimeresht[a1], Liam Reddy[b], Tanvir Hussain[b], Matti Huhtakangas[c], Nicolaie Markocsan[a], Shrikant Joshi[a]

[a] Department of Engineering Science, University West, 461 53 Trollhättan, Sweden

[b] Faculty of Engineering, The University of Nottingham, Nottingham NG7 2RD, UK

[c] M. H. Engineering AB, 691 42 Karlskoga, Sweden

Abstract

The oxidation performance of NiCrAlY and NiCrMo coatings thermally sprayed by high velocity air-fuel (HVAF) technique has been investigated in a chloridizing-oxidizing environment, with and without a KCl deposit, at 600 °C for up to 168 h. Both coatings protected the substrate in the absence of KCl due to formation of a dense Cr-rich oxide scale. In the presence of KCl, Cl^-/Cl_2 diffused through a non-protective and porous $NiCr_2O_4$ scale formed on NiCrAlY, leading to formation of volatile $CrCl_3$. On the other hand, Mo in NiCrMo stimulated the formation of a more protective Cr-rich oxide scale which increased the corrosion resistance by reducing Cl^-/Cl_2 diffusion.

Keywords: Thermal Spray Coating; NiCrAlY; NiCrMo; High-Velocity Air Fuel (HVAF); Biomass-/Waste-Fired Boiler; Fireside Corrosion

[1] Corresponding author: E-mail address: esmaeil.sadeghimeresht@hv.se (E. Sadeghimeresht)

1 Introduction

Alkali chlorides deposited on water-wall and superheater tubes are a major concern in boilers utilizing renewable fuels such as biomass and waste, as it usually leads to severe corrosion problems [1–3]. Although combustion of such fuels is reported to significantly reduce emission of greenhouse gases (e.g., CO_2) and accordingly combat global warming, degradation of the critical load-bearing components in the presence of alkali chlorides can seriously limit the thermal/electrical efficiency of the boiler [4,5]. Development of new alloys to address the problem has begun to yield diminishing returns, and consequently application of protective coatings is widely acknowledged to be the most promising option to increase the lifetime of boiler components exposed to such harsh environments [6–8]. Coatings deposited employing different techniques and utilizing varied material chemistries have been researched and deployed in boilers [9,10] but, notwithstanding the significant efforts, a dense and adherent coating that can be "maintenance-free" for an extended period remains elusive and provides the motivation for further investigation [11].

Among the various coating's chemistries, Ni-based coatings are of growing interest to be employed on the critical boiler's parts [12–17]. These coatings, with the desired level of density and adherence, can be conveniently deposited by thermal spraying techniques, e.g., atmospheric plasma spraying (APS) and high velocity oxy-fuel (HVOF) [18]. Addition of the alloying elements, i.e., Al, and Cr to Ni has been shown to ensure formation of a protective oxide scale under ordinary oxidation conditions [19,20]. However, the situation is much more complex under the oxidizing-chloridizing conditions that typically prevail in biomass/waste fired boilers. The alloying elements not only influence the type of protective scale formed but also govern the severity of internal selective attack that can occur depending on the nature of alloying elements present in the coating. The corrosive species can occasionally diffuse through the oxide layer and cause depletion of these elements [21], based on well-stablished mechanisms of "chlorine-active corrosion" [22,23] or "electrochemistry" [24,25]. While several studies have been conducted to identify the mechanisms associated with alkali chloride-induced corrosion in case of bulk materials [26,27], a better understanding of the degradation of coatings containing different alloying elements is highly desired to enable their design for superior high temperature corrosion protection.

Apart from the coating chemistry, the microstructural features in a thermal spray coating, e.g., *in situ* oxides, splat boundaries, and pores formed during the process, are also known to influence the level of corrosion protection [28]. The coatings produced by the high velocity air-fuel (HVAF) method can be distinguished by a relatively dense microstructure free from *in-situ* oxides [28–32] that are ideal from a corrosion protection standpoint. These features are realized by virtue of the lowest flame temperature and highest flame velocity (T<1800 °C, V= 700-1500 m/s) [15] that HVAF provides compared to other two conventionally used thermal spray processes of APS and HVOF [29,33]. The use of compressed air in HVAF instead of pure oxygen used in HVOF and the fact that grit-blasting procedure (to improve

coating/substrate adhesion) can be operated with the HVAF gun itself offers economic advantages well recognized by the industry.

The present work is an extension of a previous study [34] in which chlorine-induced high temperature corrosion behaviour of chromia-forming Ni21Cr and alumina-forming Ni5Al coating was investigated in 5% O_2 + 500 vppm HCl + N_2 bal. at 600 ºC for 168 h. After exposure, although Ni5Al showed better corrosion performance than Ni21Cr, lack of the stable alpha-alumina on Ni5Al led to the assumption that this coating might not withstand such a corrosive environment for a longer exposure time, hence the particular attention was paid to the chromia-forming coatings with addition of certain alloying elements such as Mo and Al. Therefore, this work aims to evaluate the role of such alloying elements on corrosion performance of the chromia-forming coatings in the similar corrosive environment (O_2+HCl) with and without KCl at 600 °C for 168 h. The improved understanding of the influence of coating composition and microstructure on corrosion performance emerging from this study has important design implications and can facilitate tailoring of highly dense and uniform microstructures with high chlorine-induced corrosion resistance. To confirm the high temperature corrosion performance of the coatings in simulated test conditions, long-term exposures in an actual boiler environment are also presently ongoing and results from this will be published later.

2 Experimental procedure

The substrate specimens used were round coupons ($\varphi_{diameter}$= 16 mm and $T_{thickness}$= 5 mm) cut from a commercially available low carbon steel 16Mo3 material (nominal composition in wt%; 0.01Cr-0.3Mo-0.5 Mn0.3Si-0.15C- Fe bal.) procured in the form of a rod. The substrates were grit blasted with alumina particles (63±10 µm) in order to roughen and clean the surfaces before coating.

The feedstock powders used were a commercially available gas-atomized powder of Ni21Cr7Al1Y (in wt%; 21.2Cr-7.3Al-0.6Y-0.2O-Ni bal.) sourced from HC Starck GmbH (Germany) (referred to as NiCrAlY hereafter) and a proprietary SiO_2-containing Ni21Cr9Mo powder supplied by M.H. Engineering AB (Sweden) (referred to as NiCrMo hereafter), both powders with particle size of 45±22 µm. The powders were selected in order to evaluate the effect of alloying elements, especially Al and Mo, on chlorine-induced corrosion behaviour of the chromia-forming coatings.

All specimens were sprayed with a M3^{TM}-HVAF spraying system (Uniquecoat, Oilville, VA, USA). The 16Mo3 rod was fixed in a horizontal rotating mandrel to first coat on the cylindrical surface, see Fig. 1. The rod was then sliced into buttons of 5 mm thickness (step A in Fig. 1) and both flat surfaces of the buttons were firstly grit blasted (step B in Fig. 1) and then HVAF sprayed (step C in Fig. 1) to ensure that the specimens were coated on all sides. The HVAF spray parameters given in Table 1 were chosen based on preliminary coating trials performed to obtain the least porous microstructure. The coatings were sprayed to a thickness of around 250 µm. The coating thickness was achieved once thickness/pass ratio was calculated after the first pass of deposition, so multiple passes (8 passes in this study as reported in Table 1) were applied to obtain the target thickness. Prior to the corrosion test, all

surfaces of the investigated samples were polished with a 0.2 μm SiC suspension to achieve a surface with R_a< 0.1 μm in order to get a uniform surface roughness on both coatings.

The corrosion tests were performed in 5 vol.% O_2 + 500 vppm HCl + N_2 for 24, 96, and 168 h at 600±1 °C, with and without KCl salt deposit using individual alumina crucibles for each specimen. The exposure set-up utilized a horizontal tube furnace with a stainless steel vessel, with the inside of the chamber entirely lined with high purity alumina. A mass flow controller was used to flow 35 cm^3/min of the synthetic gas (O_2 + HCl + N_2) through the chamber during the corrosion test. This is a simplified flue gas composition in biomass-fired boilers (e.g., forest residue, waste wood, and straw), where HCl is formed from burning high Cl-containing biomass fuels [35]. The experimental setup was based on industrial benchmark tests for biomass-fired boiler materials. A schematic diagram of the test setup used in this study is shown in Fig. 2. The test environment (e.g., gas composition and deposits) used in this study is well established and have been widely reported in literature [36–38].

A KCl suspension was prepared with ethanol and distilled water, and the deposit (~0.1 mg/cm^2) was applied on the top surface of the sample using a paintbrush. After exposure, the samples were maintained under a flow of N_2 to prevent further corrosion during cooling. Just prior to the test, the samples and the crucibles were individually weighed using a LE26P Poly Range Microbalance (Sartorius™, Massachusetts, USA). The crucibles and samples with the applied KCl deposit, if any, were also weighed together to calculate the amount of deposit placed on the surface of the sample. The samples were removed from the furnace after the test, and weighed in their individual crucibles together with any oxide scale spalled from the exposed coatings.

The growth rate of uniform and dense oxide scales is commonly assumed to be controlled by diffusion of elements through the scales [39]. A simplified analysis of this situation is carried out to show that rate control by such a process leads to the parabolic kinetics according to Eq. 1:

$$(\frac{\Delta w}{A})^2 = k_p.t \quad (1)$$

where Δw = the weight gain per unit area A (mg/cm^2), t = the oxidation time in s, and k_p = the parabolic rate constant for scaling weight gain at each temperature.

The cross-sections of the as-sprayed and exposed coatings were investigated using a QUANTA-200 FEG scanning electron microscope (FEI, Oregon, USA) equipped with X-ray energy dispersive spectroscopy (EDS). To analyse the cross sections, the as-sprayed coatings were cut slowly (at a disk speed of 300 rpm with a feed rate of 0.005 mm/min) using a diamond tipped precision saw and then cold mounted in a low shrinkage resin to prevent spallation of the formed oxide scale. The mounted samples were ground/polished to a 0.2 μm colloidal silica finish. The topographic features of the coatings were analysed using a secondary electron (SE) detector, whereas the cross-sections of the coatings were studied using backscattered electron (BSE) signals. An accelerating voltage of 20 kV in BSE and 10 kV in SE mode was used for the SEM analysis in order to improve the spatial resolution.

ImageJ software (NIH, USA) and image analysis (IA) technique were utilized to determine the extent of porosity [40] by converting the SEM (BSE mode) micrographs of the cross-sectioned coatings with horizontal field width of 100 µm into binary images, and quantifying the percentages based on grey scale contrast [30]. Five SEM images taken from each coating were used for these measurements.

A D5000 X-ray diffractometer (Siemens, Germany), equipped for grazing incidence analysis with Cr-K_α radiation (λ=0.229 nm) operating with a fixed incident angle of 1° and diffraction angle (2θ) between 25° and 80° was used to identify the phases present in the coating before and after the oxidation tests. The analysis of the diffractograms was performed with DIFFRAC.EVA using the ICDD-PDF database for phase identification.

3 Results and discussions

3.1 Characterization of as-sprayed coatings

The cross-sections of the as-sprayed NiCrAlY and NiCrMo coatings are presented in Fig. 3 (a-b). The values of porosity measured from the SEM images of the cross-sections were 0.2±0.06 and 0.4±0.1 vol.% for NiCrMo and NiCrAlY, respectively. The low amount of pores found in the coatings were promising as high corrosion protection can be expected from such dense coatings [38]. No evident gap (disbonding) between the coatings and substrates could be observed (Fig. 3) verifying that the coatings and substrates were well bonded. At higher magnification, the splat boundaries could barely be seen confirming the good cohesion among splats. A few particles that were either semi-molten or not fully deformed (flattened) to form splats were observed in the NiCrAlY coatings, whereas the NiCrMo coating microstructure was relatively more uniform. A small amount of O picked up by the EDS point analysis in NiCrAlY coatings was already reported to be sourced from the pre-existing oxygen in the powders [11] and not from the HVAF spraying process. This negligible O content confirmed that the protective scale forming elements such as Cr or/and Al were not depleted during the spraying process but preserved for oxidation protection (see EDS analysis of points A and B in Fig. 3). A higher amount of O detected in NiCrMo was attributed to the presence of SiO_2 in the coating. It is pertinent to mention that oxygen considers as a light atom, so oxygen content obtained from the EDS analysis can only be determined qualitatively and its quantitative determination contains some uncertainties.

It is widely acknowledged that coatings ideal for imparting a high corrosion resistance would be those that possess a dense structure, high adhesion to the substrate and are free from interconnected pores, which can serve as diffusion paths for the corrosive agents [11]. Such features obtained in the present work, e.g., low level of pores and oxygen in the as-sprayed coatings, high adherence of the coating to substrate and high cohesion among the splats, are all attributable to the high velocity and low temperature of the in-flight particles in the HVAF process [34].

The XRD patterns of feedstock powders and polished coatings are shown in Fig. 4 (a-b). The three primary peaks detected in case of powders in both figures corresponded to the austenitic γ-Ni(NiCr) phase. The β phase rich in Al was also observed in case of the NiCrAlY powder, and this was found to

be retained in the coating after spraying. The NiCrMo powder presented detectable amount of SiO_2, consistent with the powder constitution explained in Section 2.

The as-sprayed coatings retained the solid solution phase and corresponding oxide phases of the feedstock powders. The XRD results proved that the HVAF process did not affect the phase composition of the feedstock powders, either by forming any new phases or by eliminating the pre-existing phases. This is particularly noteworthy in case of the NiCrAlY coating, as the β phase is important to be preserved for ensuring oxidation protection [41]. The SiO_2 phase in NiCrMo might also affect the oxidation mechanism, by acting as nucleation sites to form the protective oxide layer on the surface [42]. Negligible *in situ* oxide pick up was observed after spraying of both coatings. This further confirmed the previously mentioned EDS findings which suggested that the protective scale forming alloying elements, e.g., Cr or/and Al, were not consumed during spraying but remained available for oxidation protection.

3.2 Weight change measurement

The progressive weight changes in the NiCrMo and NiCrAlY coatings exposed at 600 °C for up to168 h are shown in Fig. 5a. The results showed that a higher weight gain was recorded in the presence of KCl deposit in case of both coatings, reflecting the substantial effect of KCl on the extent of corrosion damage. The rate of weight gain increased during the early stages and then reduced as the exposure time increased. The weight gain for the NiCrMo and NiCrAlY coatings exposed to O_2 + HCl without KCl deposit was 0.31 (±0.01) and 0.37 (±0.02) mg/cm^2 respectively, whereas the values were 0.67 (±0.04) and 1.49 (±0.06) mg/cm^2 respectively with KCl after 168 h of exposure. The weight of NiCrAlY exposed to O_2 + HCl with KCl showed a significant drop in weight from 96 to 168 h, while the weight loss was very small for NiCrMo in the same period of exposure.

Fig. 5b shows the obtained data of squared weight gain in a plot of $(\Delta w/A)^2$ as a function of (t in sec.) according to Eq. (1) to obtain the values of k_p, which are given in Table 2. The lowest k_p value was measured for NiCrMo exposed without KCl ($\square 2.5\times10^{-7}$ mg^2/cm^{4}s) followed by NiCrAlY exposed without KCl ($\square 3.6\times10^{-7}$ mg^2/cm^{4}s). The highest k_p value was calculated as $\square 2.2\times10^{-5}$ mg^2/cm^{4}s for NiCrAl exposed with KCl. The calculated parabolic rate constants of the NiCrMo and NiCrAlY coatings exposed without KCl fell within the range of 3.3×10^{-9} - 2.8×10^{-7} mg^2/cm^{4}s, typically reported for chromia-forming bulk materials [43]. However, the k_p values was much higher once KCl was introduced to the environment implying that the aggressive environment facilitated formation of other corrosion products rather than chromia. It should be also noted that the parabolic rate for Cr_2O_3 scale growth may vary depending on temperature and composition.

In a previous work performed in ambient air (in the absence of HCl) [11], the above two coatings had shown much better corrosion protection behaviour in the absence of KCl, as reflected in their considerably lower recorded weight gains (0.006±0.001 and 0.13±0.1 mg/cm^2

for NiCrAlY and NiCrMo, respectively, after 168 h of exposure at 600 °C). These results confirm the strong effect of HCl on the corrosion performance of the coatings. In yet another study, adding KCl to ambient air [44] led to very high weight gains, i.e., 3.5±0.3 and 4.1±0.3 mg/cm^2 in exposed NiCrAlY and NiCrMo coatings, respectively. From all the aforementioned results, it can be summarized that, although HCl alone is more corrosive than ambient air, presence of KCl in ambient air is much more detrimental than the simultaneous presence of HCl+KCl.

In another work [34], an alumina-forming Ni5Al and a chromia-forming Ni21Cr coating showed significantly higher weight changes compared to the current NiCrAlY and NiCrMo coatings exposed to the same conditions (O_2 + HCl with KCl at 600 ºC for 168 h). The Ni5Al and Ni21Cr coatings had weight changes of 11.32±0.57 and 2.49±0.12 mg/cm^2 respectively, confirming the beneficial synergetic effect of adding alloying elements such as Al and Mo to the chromia-forming Ni21Cr coating in the present study. Although the above study had shown the alumina-forming Ni5Al coating to exhibit a lower weight change compared to the chromia-forming Ni21Cr coating due to formation of a protective Al_2O_3 scale, the results from this study demonstrate that addition of suitable alloying elements, e.g., Mo or Al, can substantially improve corrosion performance of the chromia-forming coatings.

3.3 Surface characteristics of the corrosion product

According to the XRD diffractograms shown in Fig. 6, Cr_2O_3 was only observed to form on the surface of NiCrAlY coating exposed to O_2 + HCl without KCl. $NiCr_2O_4$ along with $CrCl_3$ formed on the surface of NiCrAlY in the presence of KCl. The XRD peaks indicate the presence of Al-rich β phase confirming the potential of the NiCrAlY coating to preserve the Al content after exposure to a HCl-containing environment [11].

$NiCr_2O_4$ and MoO_3 were similarly identified on the surface of NiCrMo exposed to O_2 + HCl with and without KCl deposit. No metallic chlorides such as $MoCl_3$, $NiCl_2$, or $CrCl_3$ were found on the surface of NiCrMo in either case. In NiCrMo exposed to a KCl-containing environment, more peaks of SiO_2 could be observed compared to the XRD peaks from the exposed NiCrMo to O_2 + HCl without KCl, reflecting the contribution of SiO_2 to the formation of the oxide scale.

It has already been reported that the formation of a dense and slow-growing oxide scale is crucial for protection against corrosion at high temperature [45]. Although the coatings selected for this study were mainly chromia formers, the extent of corrosion of the coatings seems to dependent, apart from the Cr content, on the following: a) content of minor alloying elements, and b) coating microstructure in relation to the spray process used. The minor alloying elements such as Mo, Al, etc. present in the coatings can support the formation of protective chromia [46]. Indeed, the minor alloying elements have the ability to act as nucleation sites for Cr_2O_3 and form precipitates of Cr_2O_3 relatively rapidly, resulting in more stable oxide scale formation [47]. In the presence of KCl, the XRD results confirmed that Mo

was more successful than Al to support formation of a protective Cr-rich scale, as no metallic chlorides were observed on the exposed NiCrMo coating. Grabke et al. [23] and Zahs et al. [22] have also showed that alloying elements such as Mo has beneficial effects against chlorine-induced corrosion of chromia-forming alloys [35]. It was reported that the reaction of Mo and Cl_2 is less thermodynamically favoured than the reaction between Cr or Al with Cl_2, because the free energy of Mo-chlorides formation is less than the values for Cr- or Al-chlorides formation (~ -253 kJ/mol for $MoCl_3$, ~ -350 kJ/mol for $CrCl_3$, ~ -287 kJ/mol for $CrCl_2$ and ~ -525 kJ/mol for $AlCl_3$ at 600 °C).

The NiCrMo coating appeared to clearly enhance the corrosion resistance but, since both Mo and SiO_2 were present, their individual roles in enhancing the corrosion performance were difficult to isolate in the present study. Therefore, the exclusive effect of SiO_2 in increasing the corrosion resistance of the coatings in the oxidizing-chloridizing will be thoroughly investigated in a separate work.

3.4 Microstructure of formed corrosion product

3.4.1 NiCrAlY exposed to O_2 + HCl without KCl

As can be seen in Fig. 7, NiCrAlY was protective, since the coating and substrate were not notably affected. A thin layer of a protective oxide layer (Cr_2O_3 based on the previously presented XRD results) could be identified on the coating. No depletion of Cr or/and Al beneath the formed oxide layer was observed. This was indicative of the fact that HCl alone (without KCl) could not significantly damage the coating. In the Al EDS mapping, some signs of Al, most likely attributed to alumina, are seen within the splat boundaries of the coating. The O EDS mapping clearly showed a protective and thin layer of an oxide scale (~ 1 µm) formed after the exposure. Based on the XRD and EDS results, it can be noted that the oxide scale consisted of a continuous layer of a Cr_2O_3. Formation of the oxide scale did not lead to creation of a Cr-depletion zone, as seen in Cr EDS mapping in Fig. 7. As no sign of Cl was detected within the formed oxide layer (and hence the corresponding Cl map was excluded), at coating's splat boundaries and at coating/substrate interface, the formed oxide scale in a O_2+HCl environment reveals a high protection capacity. It can be concluded that, in this environment, O has a greater contribution to the corrosion behaviour than Cl.

3.4.2 NiCrAlY exposed to O_2 + HCl with KCl

It can be clearly observed in Fig. 8 that a thickness of ~ 120 µm of the coating (from its top surface) was affected by the presence of KCl. The figure also shows a mixed oxide scale/layer with a thickness of ~ 10 µm formed on the exposed coating. The EDS analysis revealed that the formed oxide layer was thick and almost porous. Al-rich and Al-depleted zones were also formed near to the top surface.

The EDS elemental mapping analysis detected signals from Al, Cr, O, Cl, and Ni in the mixed oxide scale/deposit layer. No sign of K was detected in the EDS analysis. It has been previously reported that K can contribute to "electrochemical" mechanism during the early hours of exposure [48], but this mechanism was obviously not playing any role over the long exposure (168 h) as performed in this

study since K was not detected in EDS. The simultaneous presence of Cr, Cl, and O confirmed that Cl must have diffused through the Cr-rich oxide (see Fig. 8). Beneath the oxide layer formed on the top of the coating, local enrichment of Cr at the splat boundaries could also be observed.

The dark spots seen in Fig. 8 within the region of the coating that was affected by KCl, corresponded to voids. The voids were distributed mainly beneath the top formed oxide scale. These voids could be formed by the vaporization of metallic chlorides (in this work, $CrCl_3$) which migrate outwards (towards the surface) in the form of volatile species to form the oxide scale [49], which will be further discussed in Section 3.5.

3.4.3 NiCrMo exposed to O_2 + HCl without KCl

As can be seen in Fig. 9, NiCrMo seems to be unaffected by the chloridizing-oxidizing test environment unlike NiCrAlY. Moreover, a thin and continuous layer of the oxide scale ($NiCr_2O_4$ based on the XRD graphs) entirely formed on the surface of the NiCrMo coating in the absence of KCl. Some traces of Mo could be detected in EDS elemental mapping, beneath the continuous oxide scale and within the coating where Cr was also available. The magnified SEM image of the coating (Fig. 9) revealed that no Cl could be detected within the coating, confirming the high corrosion protection imparted by the oxide scale formed. The oxide scale formed on NiCrMo was slightly thinner than that formed on NiCrAlY (Fig. 9).

3.4.4 NiCrMo exposed to O_2 + HCl with KCl

Fig. 10 shows that a thick but dense oxide layer, rich in Cr, Mo and Ni covered the entire coating surface. A slight Cr depletion was observed through the cross section, thereby suggesting that the Cr reservoir was sufficiently high to support oxide layer formation. Some sign of K was detected on the surface of the oxide scale, which can be attributed to the presence of unreacted KCl over the surface, even after 168 h of exposure. Similar to the NiCrMo coating in the absence of KCl, no sign of internal oxidation was observed within the coating's splat boundaries. The EDS analysis clearly showed the enrichment of Si in the outer parts of the coating and at the scale/coating interface, confirming the presence of SiO_2 in the corrosion product formed in the presence of KCl.

The EDS mapping shows that the thickness of the oxide layer was ~15 μm. The signals from Cl was poor in the formed oxide scale and also within the coating's splats, denoting negligible diffusion of Cl.

3.5 Proposed corrosion mechanism

In light of the obtained results, it seems that the coatings underwent both "electrochemical" and "chlorine-active corrosion" mechanisms during exposure. The two mechanisms, well described in literature [23,35,50,51], are schematically presented in Fig. 11.

According to the "electrochemical" mechanism, Cl^- diffusion through the oxide's grain boundaries occurs at the early hours (where there is only a very thin and dense oxide scale present), see Step 1 in

Fig. 11. As the exposure progresses, both mechanisms (diffusion of Cl_2 and Cl^-) could occur evolving into the next stage when the oxide becomes non-protective, thick, and porous, see Step 2 in Fig. 11. The main reason why the "chlorine-active corrosion" mechanism cannot participate in the early stage of corrosion is that the corrosion reactions which take place in this mechanism (i.e., formation of K_2CrO_4 and Cl_2 based on Eq. 2) are not thermodynamically favoured. This problem is frequently reported as one of the main drawbacks in this mechanism. In addition, inward diffusion of only Cl_2 through the cracks and the pores of the scale (while diffusion of O_2 and gaseous metallic chloride could be also possible) is also not well explained in this mechanism.

$$Cr_2O_3(s) + 4KCl(s) + \frac{5}{2}O_2(g) = 2K_2CrO_4(s) + 2Cl_2(g) \quad (2)$$

$\Delta G_f^0(K_2CrO_4) \approx 73.8\ kJ/mol\ at\ 600\ ℃$

As Cl was detected within the oxide scales formed on both coatings, it could be assumed that corrosion was initiated by the reaction of KCl with Cr_2O_3, forming K_2CrO_4 and Cl^- based on Eqs. (3-7) [48,52], shown in Step 1, Fig. 11. As Cl^- is smaller than Cl_2, it has higher mobility in the oxide scale's grain boundaries and coating's splat boundaries [53]. Once Cl^- reaches the interface, it reacts with transition metal ions (for instance, Cr) formed by the oxidation of coating as suggested in Eq. 3;

Scale/coating interface:

$$Cr = Cr^{2+}(oxide) + 2e^- \quad (3)$$

The reaction that occurs on the scale surface is:

$$\frac{1}{2}Cr_2O_3 + 4KCl(s) + \frac{5}{2}O_2(g) + 2e^- = K_2CrO_4(s) + 2Cl^- \quad (4)$$

And at the locations where Cl^- and Cr^{2+} meet each other within the coating:

$$Cr^{2+} + Cl^- = CrCl_2\ (s) \quad (5)$$

$$CrCl_2\ (s) = CrCl_2\ (g) \quad (6)$$

The sum these reactions becomes (for the case of Cr oxidation):

$$\frac{1}{3}Cr_2O_3 + 2KCl(s) + \frac{3}{2}O_2(g) + Cr = K_2CrO_4(s) + \frac{2}{3}CrCl_3\ (g) \quad (7)$$

$\Delta G_f^0(K_2CrO_4) \approx -292.6\ kJ/mol\ at\ 600\ ℃$

It should be noted that the "electrochemical" mechanism can be interrupted if KCl was completely consumed as there would not be any reservoir to promote Cl^- formation. However, the SEM results confirmed that KCl was still present on the exposed coatings even after exposure, meaning that the environment remained oxidizing-chloridizing during the course of exposure.

The formed solid chlorides have considerable equilibrium vapour pressures (see Eq. 6), evaporate readily, and diffuse upward towards gas–oxide scale interface, see Step 2 in Fig. 11. When the sufficient pO_2 is available, the gaseous chlorides react with the available oxygen to form solid oxides, releasing Cl_2, see Eqs. (8-12) [35], e.g.:

$$NiCl_2(g) + \frac{1}{2}O_2(g) = NiO(s) + Cl_2(g) \qquad \Delta G_f^0(NiO) \approx -50.9\ kJ/mol\ at\ 600\ ℃ \qquad (8)$$

$$SiCl_4(g) + O_2(g) = SiO_2(s) + 2Cl_2(g) \qquad \Delta G_f^0(SiO_2) \approx -205.4\ kJ/mol\ at\ 600\ ℃ \qquad (9)$$

$$2CrCl_3(g) + \frac{3}{2}O_2(g) = Cr_2O_3(s) + 3Cl_2(g) \qquad \Delta G_f^0(Cr_2O_3) \approx -255.6\ kJ/mol\ at\ 600\ ℃ \qquad (10)$$

$$2AlCl_3(g) + 3/2O_2(g) = Al_2O_3(s) + 3Cl_2(g) \qquad \Delta G_f^0(Al_2O_3) \approx -319.9\ kJ/mol\ at\ 600\ ℃ \qquad (11)$$

$$MoCl_3(g) + 3/2O_2(g) = MoO_3(s) + 3/2Cl_2(g) \qquad \Delta G_f^0(MoO_3) \approx -349.3\ kJ/mol\ at\ 600\ ℃ \qquad (12)$$

Once Cl_2 formed, as shown in the above reactions, it may diffuse through defects (mainly pores and cracks) in the oxide scale towards the scale-coating interface and even further towards the coating-substrate interface (where pO_2 is low) via "chlorine-active corrosion" mechanism. Depending upon the available alloying elements in the coatings which were Ni, Cr, Al, and Mo in the present study, solid metal chlorides which are thermodynamically stable could form after reacting with Cl_2 (where pO_2 is high), see suggested in Eqs. 13-17.

$$Ni\ (s) + Cl_2\ (g) = NiCl_2\ (s) \qquad \Delta G_f^0(NiCl_2) \approx -173.9\ kJ\ at\ 600\ ℃ \qquad (13)$$

$$Mo\ (s) + 3/2Cl_2\ (g) = MoCl_3\ (s) \qquad \Delta G_f^0(MoCl_3) \approx -253.7\ kJ\ at\ 600\ ℃ \qquad (14)$$

$$Cr\ (s) + 3/2Cl_2\ (g) = CrCl_3\ (s) \qquad \Delta G_f^0(CrCl_3) \approx -371.6\ kJ\ at\ 600\ ℃ \qquad (15)$$

$$Al\ (s) + 3/2Cl_2\ (g) = AlCl_3\ (s) \qquad \Delta G_f^0(AlCl_3) \approx -525.6\ kJ\ at\ 600\ ℃ \qquad (16)$$

$$Si\ (s) + 2Cl_2\ (g) = SiCl_4\ (s) \qquad \Delta G_f^0(SiCl_4) \approx -547.1\ kJ\ at\ 600\ ℃ \qquad (17)$$

Based on the thermodynamics and Gibbs free energy of formation of the metallic chlorides, $AlCl_3$ is more thermodynamically favoured than the other metallic chlorides particularly $MoCl_3$ (based on Eqs. 13-17). Even once $MoCl_3$ forms, transformation of such chloride to oxide (MoO_3) is again more thermodynamically favoured than transformation of $AlCl_3$ to Al_2O_3 (see Eqs. 8-12). This proved that the contribution of Mo in the oxide scale to provide a better corrosion protection was higher than that of Al.

The weight change of NiCrMo was also significantly lower than that of NiCrAlY due to the formation of a protective $NiCr_2O_4$ scale, which prevented the formation of volatile $NiCl_2$. Mo did not interrupt the formation of the $NiCr_2O_4$ scale on the NiCrMo coating as no $MoCl_3$ was detected, while Al in NiCrAlY was not successful enough, as formation of $AlCl_3$ was thermodynamically the most favoured reaction among the other alloying elements.

Fig. 10 also indicates the potential protective effect of a dense SiO_2 scale in oxidizing-chloridizing environments at 600 °C. The effect of SiO_2 in NiCrMo was clearly stronger than the effect of Al in NiCrAlY. It is because the chlorine partial pressure (pCl_2) for the formation of volatile $SiCl_4$ is always higher than that for the formation of volatile $AlCl_3$ [54]. If cracks are present in the oxide scale, the formation of $SiCl_4$ may also take place at the oxide/coating interface. The formation of $SiCl_4$ impedes healing of the damaged oxide scale. Since the reaction of $SiCl_4$ to stable SiO_2 and Cl_2 is relatively slow, a circular mechanism, similar to those discussed for other elements, can be excluded, in particular in the presence of a very thin protective SiO_2 layer.

Another important finding was the increased level of voids in the exposed coatings (in particular NiCrAlY), which is consistent with the findings of several other studies [50,55] and explained in terms of diffusional processes. The outward diffusion of elements such as Al and Cr left a void-rich region that act as open channels for enhanced transport of Cl_2, accordingly high vaporization of the formed metallic chlorides. Consequently, deep internal corrosion could occur (120 µm of the NiCrAlY coating was affected, see Fig. 8). Fig. 8 provides a better insight into processes that occur beneath the KCl deposit, with some of the residual KCl still being retained on the coatings surface, (although some of it could be lost during material preparation and replaced by the mounting resin, leaving the formed oxide, as scattered areas within the mounting resin). Indeed, diffusion of Cr or Al towards the surface of the NiCrMo or NiCrAlY coating could be evidenced with the voids formed in the Ni-rich areas. Cl was not only detected in the oxide/coating interface but also within the coating, most commonly in the pores. This proves that Cl may diffuse along the splat boundaries and structural defects of thermal spray coatings, such as interconnected pores, that exist and form during spraying process within the coatings, creating high pCl_2 regions near the substrate surface [21,56].

5 Conclusions

High temperature chlorine-induced corrosion behaviour of HVAF thermal-sprayed NiCrAlY and NiCrMo coatings was investigated in 5 vol.% O_2 + 500 vppm HCl + N_2 with and without KCl salt deposit at 600 °C for 168 h. The coatings subjected to corrosion tests revealed a strong correlation between the alloying elements and corrosion. The coatings demonstrated low corrosion attack in the O_2+HCl environment without KCl, however the corrosion protection was less in the presence of KCl. While both coatings were chromia formers in the test condition, NiCrAlY showed higher weight gain compared to NiCrMo, verifying the beneficial effect of Mo to reduce the corrosion, especially in the presence of KCl. In the O_2+HCl environment with KCl, preferential removal of Al from the corrosion front in NiCrAlY was observed due to the formation of a porous and non-protective Cr-rich scale, which facilitated the formation of volatile metallic chlorides such as $CrCl_3$ and $AlCl_3$. Chloride attack was particularly rapid in the vicinity of coating's splat boundaries where the oxides were present. Cl^- and Cl_2 could diffuse through the grain boundaries and pores of the formed oxide scale respectively, forming

metal chlorides and accelerating the corrosion. In the presence of KCl, Mo supported formation of the protective oxide scale rich in Cr, which reduced the formation of volatile $CrCl_3$.

Acknowledgment

Financial support of the Knowledge Foundation for the SCoPe project (RUN 20160201) and Västra Götalandsregionen (VGR) for the PROSAM project (RUN 2016-01489) are highly acknowledged. The authors would like to thank Dr. Mingwen Bai, Mr. Jonas Olsson, Mr. Stefan Björklund, and Mr. Kenneth Andersson for their valuable help and advice in processing and characterization of the HVAF coatings in this study. The Swedish High Temperature Corrosion Centre (HTC) at Chalmers University of Technology is appreciated for the help in the XRD/SEM/EDS analysis.

Reference

1. A. Demirbas, Potential applications of renewable energy sources, biomass combustion problems in boiler power systems and combustion related environmental issues, *Prog. Energy Combust. Sci.* 31 (2) (2005) 171–192.
2. A.A. Khan et al., Biomass combustion in fluidized bed boilers: Potential problems and remedies, *Fuel Process. Technol.* 90 (1) (2009) 21–50.
3. L. Baxter, Biomass-coal co-combustion: opportunity for affordable renewable energy, *Fuel* 84 (10) (2005) 1295–1302.
4. S. Karlsson, L.-E. Åmand, and J. Liske, Reducing high-temperature corrosion on high-alloyed stainless steel superheaters by co-combustion of municipal sewage sludge in a fluidised bed boiler, *Fuel* 139 (2015) 482–493.
5. G. Balan, M. Losurdo, and H. Spliethoff, Experimental Study of High-Temperature Chlorine-Induced Corrosion in Dependence of Gas Velocity, *Energy Fuels* 27 (10) (2013) 5628–5639.
6. M. Oksa et al., Nickel-based HVOF coatings promoting high temperature corrosion resistance of biomass-fired power plant boilers, *Fuel Process. Technol.* 125 (2014) 236–245.
7. H. Kassman et al., Two strategies to reduce gaseous KCl and chlorine in deposits during biomass combustion - Injection of ammonium sulphate and co-combustion with peat, *Fuel Process. Technol.* 105 (2013) 170–180.
8. T. Varis et al., High temperature corrosion of thermally sprayed NiCr and FeCr coatings covered with a KCl-K2SO4 salt mixture, *Surf. Coat. Technol.* 265 (2015) 235–243.
9. M. Oksa, T. Varis, and K. Ruusuvuori, Performance testing of iron based thermally sprayed HVOF coatings in a biomass-fired fluidised bed boiler, *Surf. Coat. Technol.* 251 (2014) 191–200.
10. M. Oksa, J. Metsäjoki, and J. Kärki, Thermal Spray Coatings for High-Temperature Corrosion Protection in Biomass Co-Fired Boilers, *J. Therm. Spray Technol.* 24 (1–2) (2014) 194–205.
11. E. Sadeghimeresht et al., Isothermal oxidation of HVAF-sprayed Ni-based chromia, alumina and mixed-oxide scale forming coatings in ambient air, *Surf. Coat. Technol.* 316 (2017) 10–21.
12. E. Sadeghimeresht, N. Markocsan, and S. Joshi, Isothermal oxidation behavior of HVAF-sprayed Ni and NiCr coatings in H2-H2O environment, *Surf. Coat. Technol.* 317 (2017) 17–25.
13. X.-Z. Li et al., Investigations on the behavior of laser cladding Ni-Cr-Mo alloy coating on TP347H stainless steel tube in HCl rich environment, *Surf. Coat. Technol.* 232 (2013) 627–639.
14. E. Sadeghimeresht et al., Oxidation Behavior of HVAF-Sprayed NiCoCrAlY Coating in H2–H2O Environment, *Oxid. Met.* 86 (3–4) (2016) 299–314.
15. N. Bala, H. Singh, and S. Prakash, Accelerated hot corrosion studies of cold spray Ni–50Cr coating on boiler steels, *Mater. Des.* 31 (1) (2010) 244–253.
16. R. Mousavi, M.E. Bahrololoom, and F. Deflorian, Preparation, corrosion, and wear resistance of Ni- Mo/Al composite coating reinforced with Al particles, *Mater. Des.* 110 (2016) 456–465.
17. A.J. López et al., High-temperature corrosion behavior of Ni–50Cr coating deposited by high velocity oxygen–fuel technique on low alloy ferritic steel, *Mater. Des.* 59 (2014) 94–102.

18. M. Oksa, S. Tuurna, and T. Varis, Increased Lifetime for Biomass and Waste to Energy Power Plant Boilers with HVOF Coatings: High Temperature Corrosion Testing Under Chlorine-Containing Molten Salt, *J. Therm. Spray Technol.* 22 (5) (2013) 783–796.
19. Y.S. Li, M. Spiegel, and S. Shimada, Corrosion behaviour of various model alloys with NaCl–KCl coating, *Mater. Chem. Phys.* 93 (1) (2005) 217–223.
20. Y. Kawahara and M. Kira, Corrosion Prevention of Waterwall Tube by Field Metal Spraying in Municipal Waste Incineration Plants, *CORROSION* 53 (3) (1997) 241–251.
21. K.A. Habib et al., Performance of NiCrAlY Coatings Deposited by Oxyfuel Thermal Spraying in High Temperature Chlorine Environment, *J. Mater. Eng. Perform.* 23 (10) (2014) 3511–3522.
22. A. Zahs, M. Spiegel, and H. Grabke, The influence of alloying elements on the chlorine-induced high temperature corrosion of Fe-Cr alloys in oxidizing atmospheres, *Mater. Corros.* 50 (10) (1999) 561–578.
23. H.J. Grabke, E. Reese, and M. Spiegel, The effects of chlorides, hydrogen chloride, and sulfur dioxide in the oxidation of steels below deposits, *Corros. Sci.* 37 (7) (1995) 1023–1043.
24. J. Pettersson et al., KCl Induced Corrosion of a 304-type Austenitic Stainless Steel at 600°C; The Role of Potassium, *Oxid. Met.* 64 (1–2) (2005) 23–41.
25. G. Sorell, The role of chlorine in high temperature corrosion in waste-to-energy plants, *Mater. High Temp.* 14 (3) (1997) 207–220.
26. S. Enestam et al., Are NaCl and KCl equally corrosive on superheater materials of steam boilers?, *Fuel* 104 (2013) 294–306.
27. J. Metsäjoki, E. Huttunen-Saarivirta, and T. Lepistö, Elevated-temperature corrosion of uncoated and aluminized 9–12% Cr boiler steels beneath KCl deposit, *Fuel* 133 (Supplement C) (2014) 173–181.
28. E. Sadeghimeresht, N. Markocsan, and P. Nylén, A Comparative Study of Corrosion Resistance for HVAF-Sprayed Fe- and Co-Based Coatings, *Coatings* 6 (2016) 16.
29. E. Sadeghimeresht, N. Markocsan, and P. Nylén, A Comparative Study on Ni-Based Coatings Prepared by HVAF, HVOF, and APS Methods for Corrosion Protection Applications, *J. Therm. Spray Technol.* 25 (8) (2016) 1604–1616.
30. E. Sadeghimeresht et al., Corrosion performance of bi-layer Ni/Cr2C3–NiCr HVAF thermal spray coating, *Appl. Surf. Sci.* 369 (2016) 470–481.
31. E. Sadeghimeresht, N. Markocsan, and P. Nylén, Microstructural and electrochemical characterization of Ni-based bi-layer coatings produced by the HVAF process, *Surf. Coat. Technol.* 304 (2016) 606–619.
32. E. Sadeghimeresht, N. Markocsan, and P. Nylén, Microstructure Effect of Intermediate Coat Layer on Corrosion Behavior of HVAF-Sprayed Bi-Layer Coatings, *J. Therm. Spray Technol.* 26 (1–2) (2017) 243–253.
33. E. Sadeghimeresht, N. Markocsan, and P. Nylén, Microstructural characteristics and corrosion behavior of HVAF- and HVOF-sprayed Fe-based coatings, *Surf. Coat. Technol.* 318 (2017) 365–373.
34. E. Sadeghimeresht et al., Chlorine-induced high temperature corrosion of HVAF-sprayed Ni-based alumina and chromia forming coatings, *Corros. Sci.* 132 (2018) 170–184.
35. A. Zahs, M. Spiegel, and H.J. Grabke, Chloridation and oxidation of iron, chromium, nickel and their alloys in chloridizing and oxidizing atmospheres at 400-700°C, *Corros. Sci.* 42 (6) (2000) 1093–1122.
36. M. Bai, L. Reddy, and T. Hussain, Experimental and thermodynamic investigations on the chlorine-induced corrosion of HVOF thermal sprayed NiAl coatings and 304 stainless steels at 700 °C, *Corros. Sci.* (2018).
37. T. Dudziak et al., Fireside corrosion degradation of ferritic alloys at 600°C in oxy-fired conditions, *Corros. Sci.* 79 (2014) 184–191.
38. T. Hussain et al., Fireside corrosion degradation of HVOF thermal sprayed FeCrAl coating at 700–800°C, *Surf. Coat. Technol.* 268 (2015) 165–172.
39. G.Y. Lai, *High-Temperature Corrosion and Materials Applications*, *ASM International*, (2007).
40. C.A. Schneider, W.S. Rasband, and K.W. Eliceiri, NIH Image to ImageJ: 25 years of image analysis, *Nat. Methods* 9 (7) (2012) 671–675.

41. C. Kaplin and M. Brochu, Effects of water vapor on high temperature oxidation of cryomilled NiCoCrAlY coatings in air and low-SO2 environments, *Surf. Coat. Technol.* 205 (17–18) (2011) 4221–4227.
42. Y.S. Li, Y. Niu, and M. Spiegel, High temperature interaction of Al/Si-modified Fe–Cr alloys with KCl, *Corros. Sci.* 49 (4) (2007) 1799–1815.
43. S. Cruchley et al., Chromia layer growth on a Ni-based superalloy: Sub-parabolic kinetics and the role of titanium, *Corros. Sci.* 75 (Supplement C) (2013) 58–66.
44. R. Jafari et al., KCl-Induced High-Temperature Corrosion Behavior of HVAF-Sprayed Ni-Based Coatings in Ambient Air, *J. Therm. Spray Technol.* 27 (3) (2018) 500–511.
45. V. Trindade, H.-J. Christ, and U. Krupp, Grain-Size Effects on the High-Temperature Oxidation Behaviour of Chromium Steels, *Oxid. Met.* 73 (5–6) (2010) 551–563.
46. D.W. Yun et al., The effects of the minor alloying elements Al, Si and Mn on the cyclic oxidation of Ni–Cr–W–Mo alloys, *Corros. Sci.* 83 (2014) 176–188.
47. F.H. Stott, Influence of alloy additions on oxidation, *Mater. Sci. Technol.* 5 (8) (1989) 734–740.
48. N. Israelsson et al., A Microstructural and Kinetic Investigation of the KCl-Induced Corrosion of an FeCrAl Alloy at 600 °C, *Oxid. Met.* 84 (1–2) (2015) 105–127.
49. T. Jonsson et al., Microstructural Investigation of the HCl-Induced Corrosion of the Austenitic Alloy 310S (52Fe26Cr19Ni) at 500 °C, *Oxid. Met.* 81 (5–6) (2014) 575–596.
50. M.A. Uusitalo, P.M.J. Vuoristo, and T.A. Mäntylä, High temperature corrosion of coatings and boiler steels below chlorine-containing salt deposits, *Corros. Sci.* 46 (6) (2004) 1311–1331.
51. M. Spiegel, A. Zahs, and H.J. Grabke, Fundamental aspects of chlorine induced corrosion in power plants, *Mater. High Temp.* 20 (2) (2003) 153–159.
52. Y. Shu, F. Wang, and W. Wu, Corrosion Behavior of Pure Cr with a Solid NaCl Deposit in O2 Plus Water Vapor, *Oxid. Met.* 54 (5–6) (2000) 457–471.
53. M.A. Olivas-Ogaz et al., Microstructural Study of the Influence of KCl and HCl on Preformed Corrosion Product Layers on Stainless Steel, *Oxid. Met.* 87 (5–6) (2017) 801–811.
54. R. Bender and M. Schütze, The role of alloying elements in commercial alloys for corrosion resistance in oxidizing-chloridizing atmospheres Part II: Experimental investigations, *Mater. Corros.* 54 (9) (2003) 652–686.
55. M.A. Uusitalo, P.M.J. Vuoristo, and T.A. Mäntylä, High temperature corrosion of coatings and boiler steels in oxidizing chlorine-containing atmosphere, *Mater. Sci. Eng. A* 346 (1) (2003) 168–177.
56. Z. Pala et al., Laser Clad and HVOF-Sprayed Stellite 6 Coating in Chlorine-Rich Environment with KCl at 700 °C, *Oxid. Met.* (2017) 1–23.

Figures and Tables Captions:

Table:

Table 1. HVAF process parameters used to spray the NiCrMo and NiCrAlY coatings

Table 2. Weight gain parabolic rate constant (k_p) determined from Fig. 4b

Figures:

Fig. 1. Schematic of the procedure followed to produce the fully coated specimens. The 16Mo3 rod with the length of 500 mm and diameter of 16 mm was firstly grit blasted and then coated using the HVAF process. The coated rod was then sliced to small buttons with thickness of 5 mm (step A). The two flat surfaces (top and bottom) of the buttons were grit blasted (step B) and then coated (step C). Especial attention was paid to the corner of buttons in order to avoid any damage during cutting, grit blasting and spraying.

Fig. 2. Schematic diagram of the controlled-atmosphere high temperature corrosion rig.

Fig. 3. Back-scattered SEM micrographs of cross-sections of the as-sprayed coatings, coating/substrate interfaces, and the corresponding EDS point analysis, a) NiCrAlY, and b) NiCrMo.

Fig. 4. XRD patterns of the NiCrAlY and NiCrMo powders and corresponding polished coatings.

Fig. 5. a) Weight gain of the exposed NiCrAlY and NiCrMo coatings in 5%O_2 + 500ppm HCl + N_2 with and without KCl deposit up to 168 h at 600 °C, and b) squared of weight gain versus time (h).

Fig. 6. XRD patterns of the exposed NiCrMo and NiCrAlY coatings in 5%O_2 + 500ppm HCl + N_2 for 168 h at 600 °C with and without KCl deposit.

Fig. 7. Cross-sectional SEM micrographs (BSE) and EDS elemental mapping analysis of the NiCrAlY coating oxidized in 5%O_2 + 500ppm HCl + N_2 without KCl deposit for 168 h at 600 °C.

Fig. 8. Cross-sectional SEM micrographs (BSE) and EDS elemental mapping analysis of the NiCrAlY coating oxidized in 5%O_2 + 500ppm HCl + N_2 with KCl deposit for 168 h at 600 °C.

Fig. 9. Cross-sectional SEM micrograph (BSE) and EDS elemental mapping analysis of the NiCrMo coating oxidized in 5%O_2 + 500ppm HCl + N_2 without KCl deposit for 168 h at 600 °C.

Fig. 10. Cross-sectional SEM micrograph (BSE) and EDS elemental mapping analysis of the NiCrMo coating oxidized in 5%O_2 + 500ppm HCl + N_2 with KCl deposit for 168 h at 600 °C.

Fig. 11. Schematic of the proposed corrosion mechanisms in the coatings exposed to 5%O_2 + 500ppm HCl + N_2 with KCl for 168 h at 600 °C.

Tables

Table 1. HVAF process parameters used to spray the NiCrMo and NiCrAlY coatings

Variables	
Nozzle type	For NiCrAlY: 3L2G For NiCrMo: 4L2G
Air pressure, MPa	0.8
Fuel 1 pressure-Propane, MPa	0.7
Fuel 2 pressure-Propane, MPa	0.7
Carrier gas pressure-N_2, MPa	0.4
Feed rate, g/min	150
Pass velocity, m/min	50
Pass spacing, mm/rev.	5
Spray distance, mm	300
Number of Passes	8

Table 2. Weight gain parabolic rate constant (k_p) determined from Fig. 4b

Coating/environment	k_p (mg^2/cm^4s)
NiCrAlY without KCl	3.6×10^{-7}
NiCrAlY with KCl*	2.2×10^{-5}
NiCrMo without KCl	2.5×10^{-7}
NiCrMo with KCl	1.3×10^{-6}

* K_p value for NiCrAlY exposed to KCl was measured within the exposure period from 0 to 96 h to avoid the interference by the weight change drop observed from 96 h to 168 h.

Figures

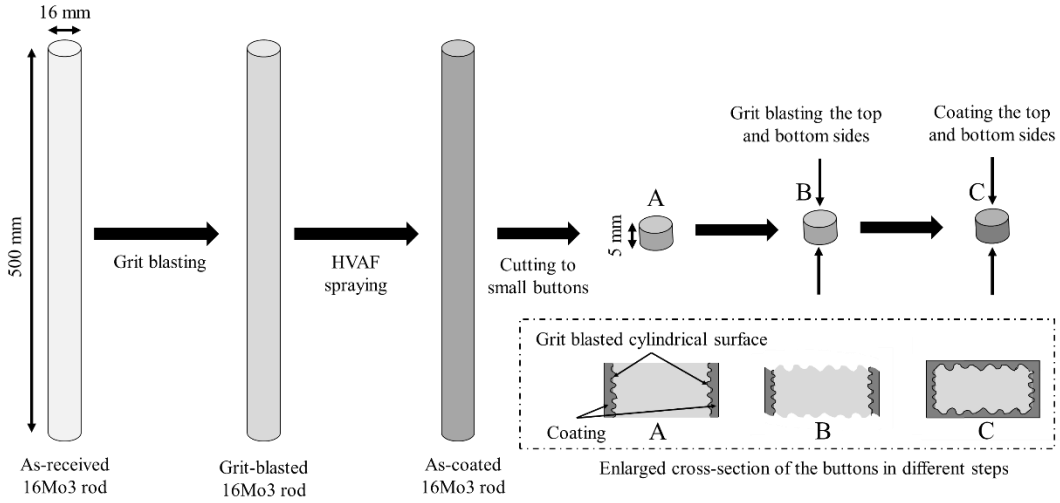

Fig. 1. Schematic of the procedure followed to produce the fully coated specimens. The 16Mo3 rod with the length of 500 mm and diameter of 16 mm was firstly grit blasted and then coated using the HVAF process. The coated rod was then sliced to small buttons with thickness of 5 mm (step A). The two flat surfaces (top and bottom) of the buttons were grit blasted (step B) and then coated (step C). Especial attention was paid to the corner of buttons in order to avoid any damage during cutting, grit blasting and spraying.

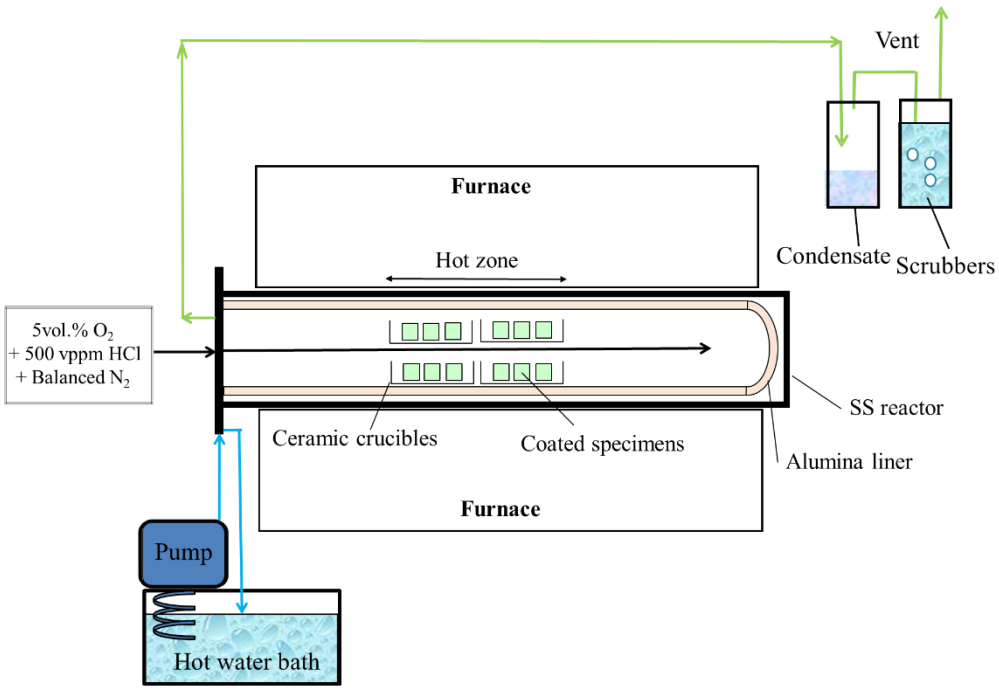

Fig. 2. Schematic diagram of the controlled-atmosphere high temperature corrosion rig.

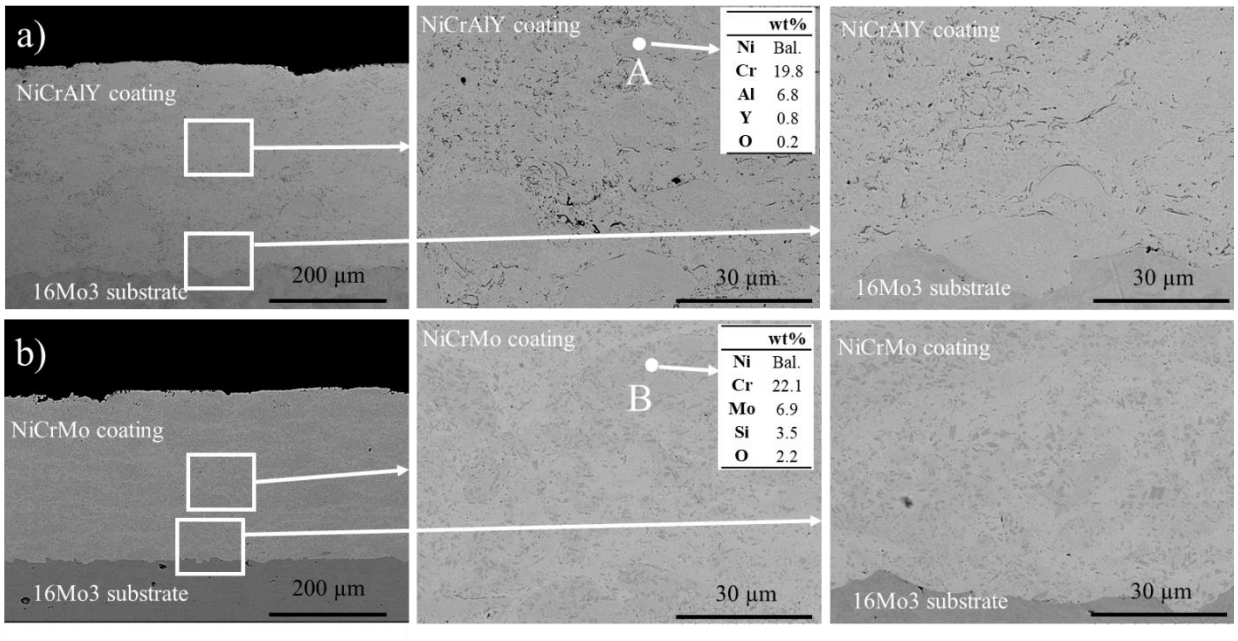

Fig.3. Back-scattered SEM micrographs of cross-sections of the as-sprayed coatings, coating/substrate interfaces, and the corresponding EDS point analysis, a) NiCrAlY, and b) NiCrMo.

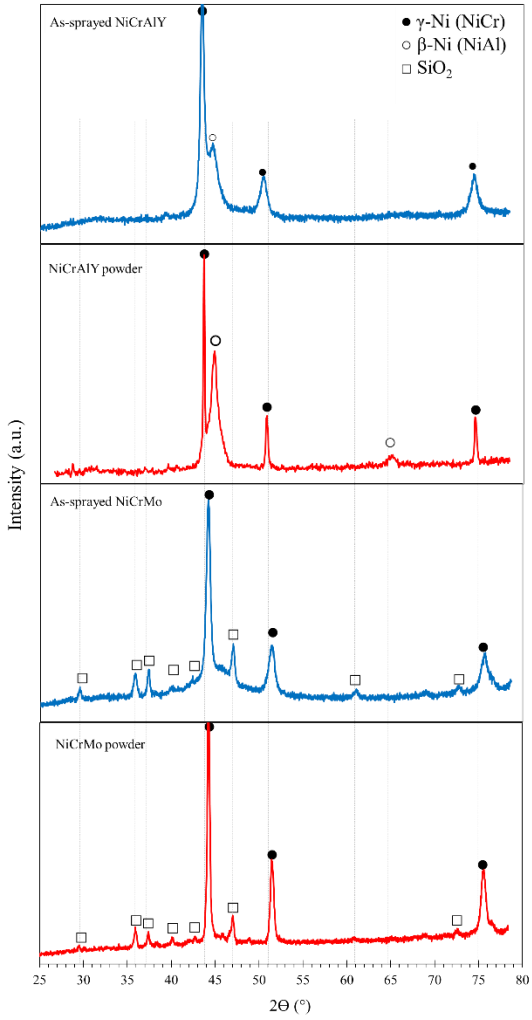

Fig. 4. XRD patterns of the NiCrAlY and NiCrMo powders and the corresponding polished coatings.

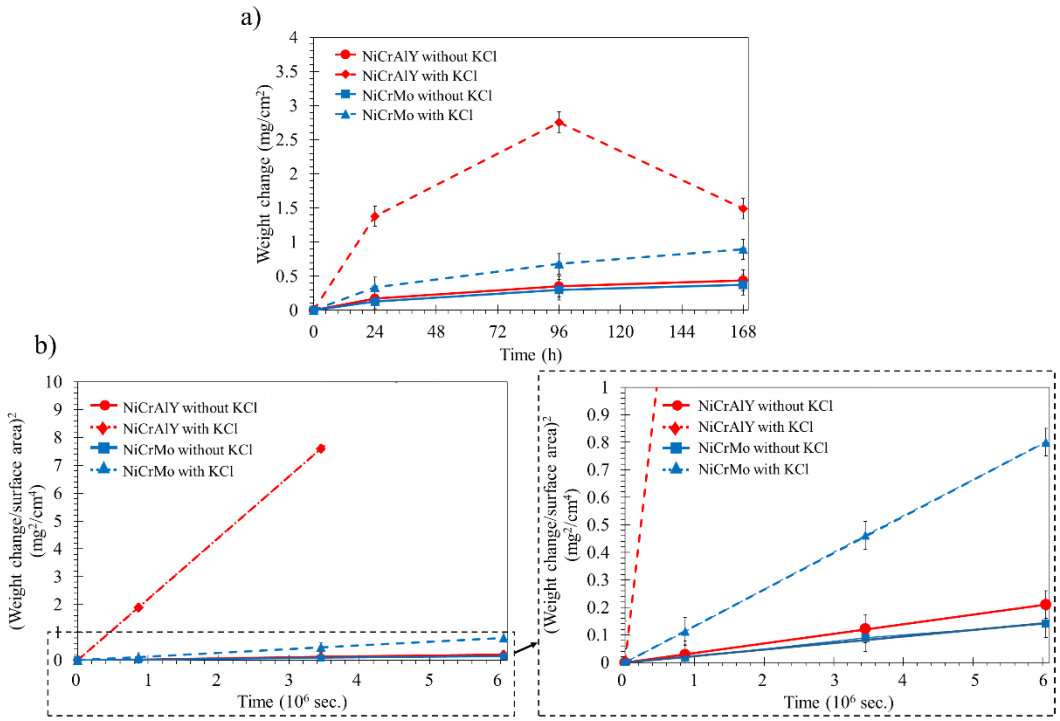

Fig. 5. a) Weight gain of the exposed NiCrAlY and NiCrMo coatings in 5%O_2 + 500ppm HCl + N_2 with and without KCl deposit up to 168 h at 600 °C, and b) squared of weight gain versus time (h).

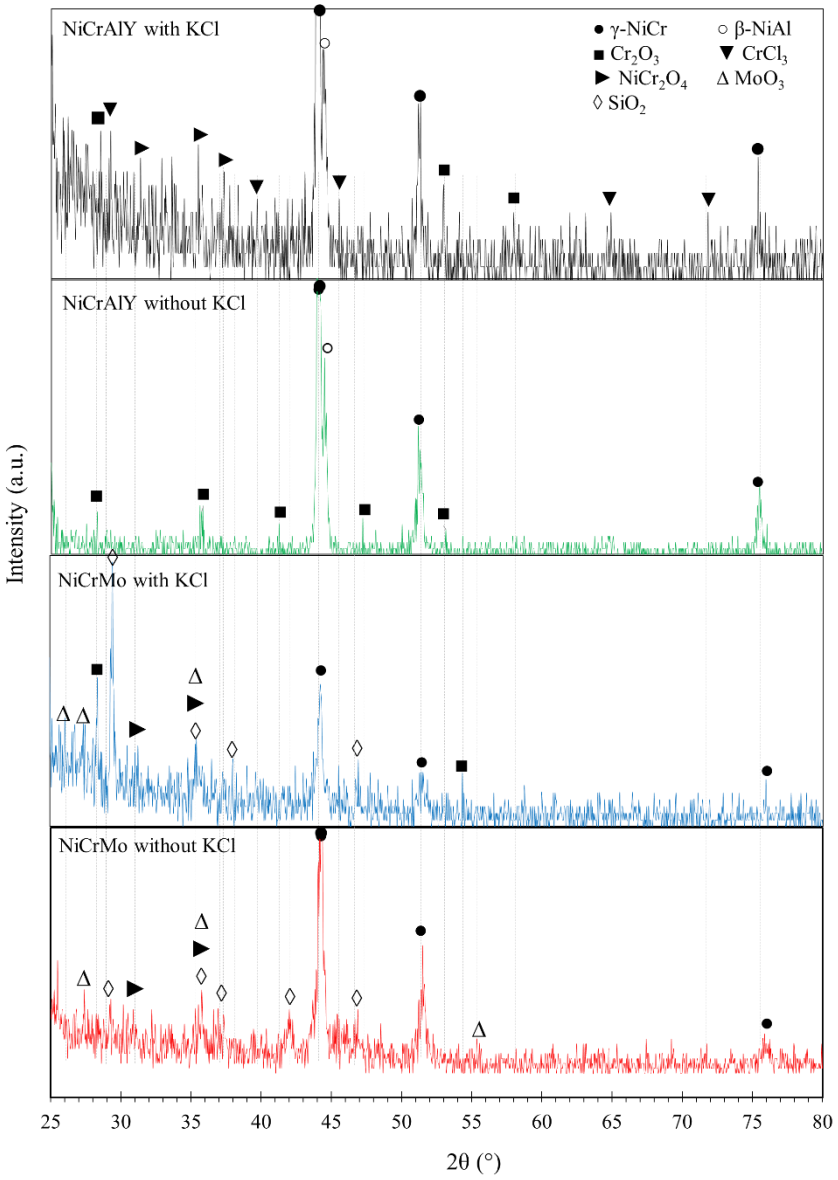

Fig. 6. XRD patterns of the exposed coatings in 5%O_2 + 500ppm HCl + N_2 for 168 h at 600 °C with and without KCl deposit.

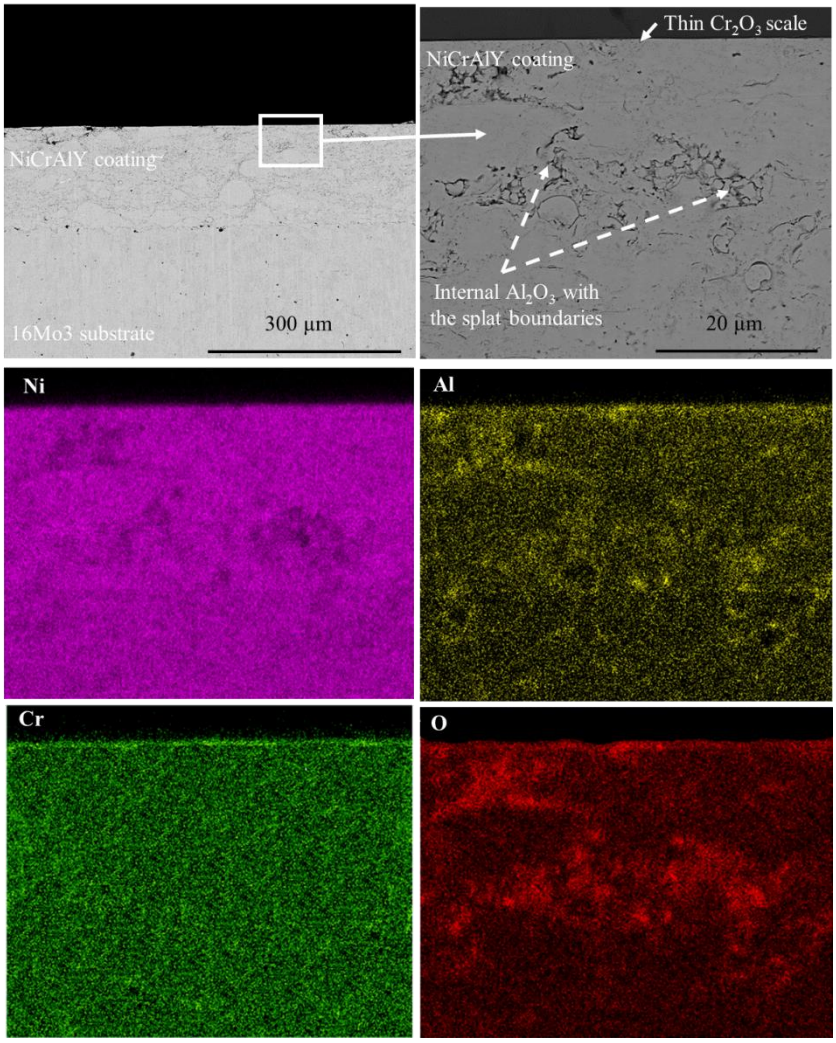

Fig. 7. Cross-sectional SEM micrographs (BSE) and EDS elemental mapping analysis of the NiCrAlY coating oxidized in 5%O_2 + 500ppm HCl + N_2 without KCl deposit for 168 h at 600 °C.

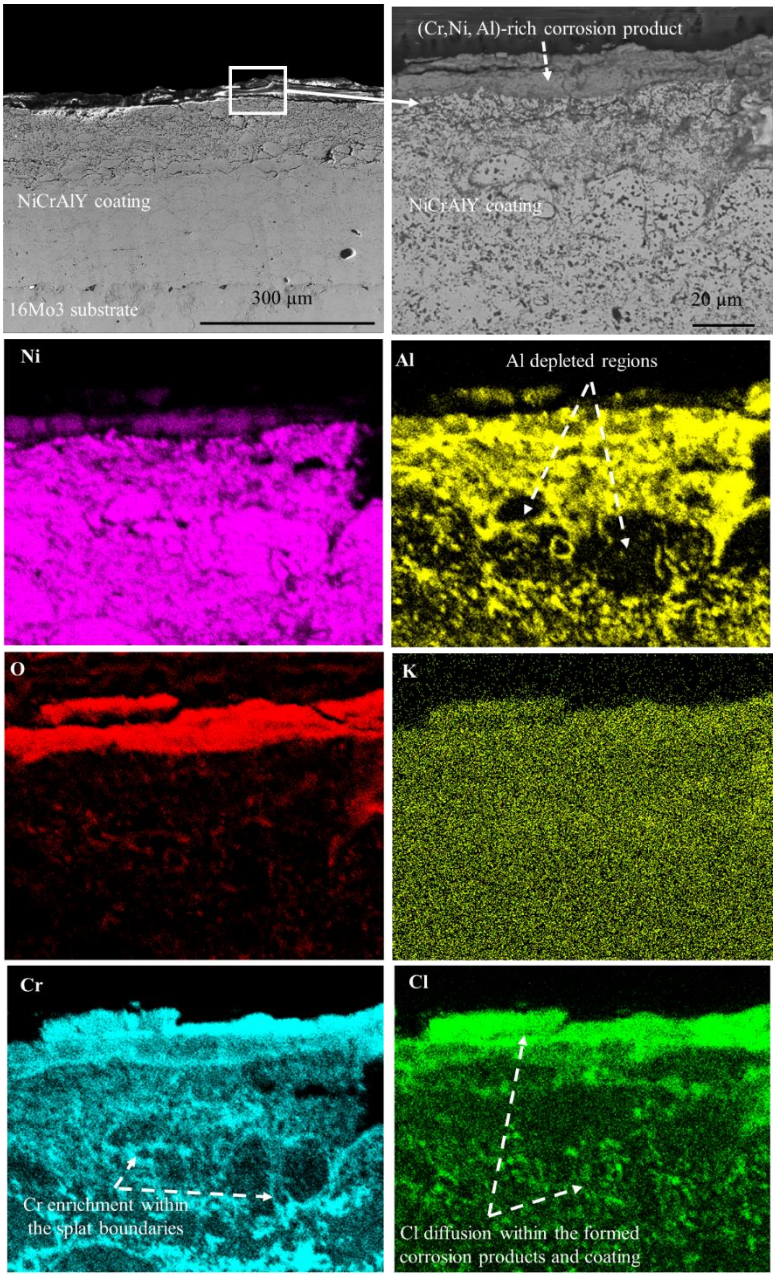

Fig. 8. Cross-sectional SEM micrographs (BSE) and EDS elemental mapping analysis of the NiCrAlY coating oxidized in 5%O_2 + 500ppm HCl + N_2 with KCl deposit for 168 h at 600 °C.

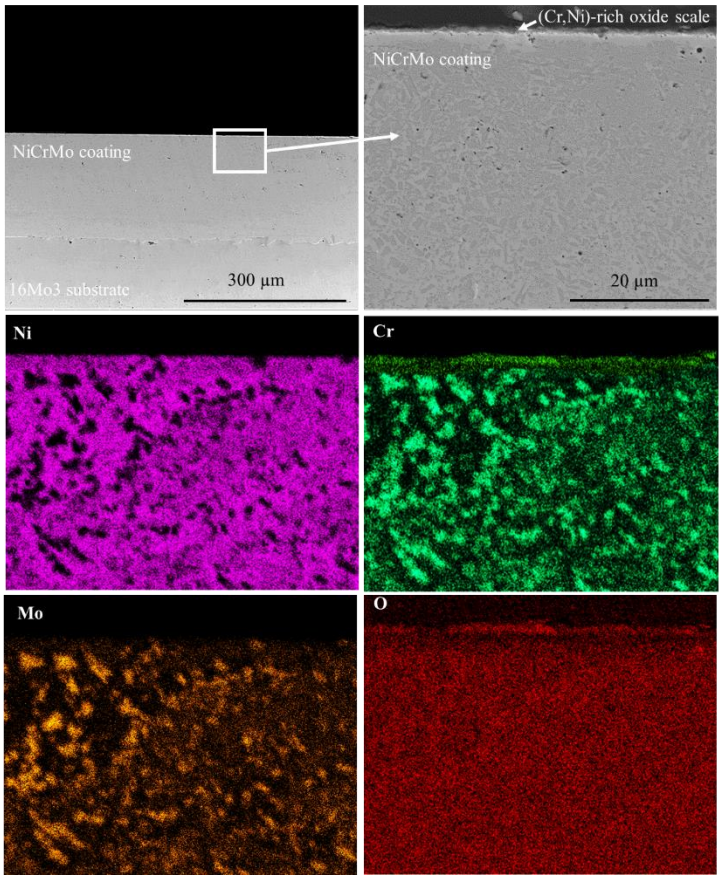

Fig. 9. Cross-sectional SEM micrograph (BSE) and EDS elemental mapping analysis of the NiCrMo coating oxidized in 5%O_2 + 500ppm HCl + N_2 without KCl deposit for 168 h at 600 °C.

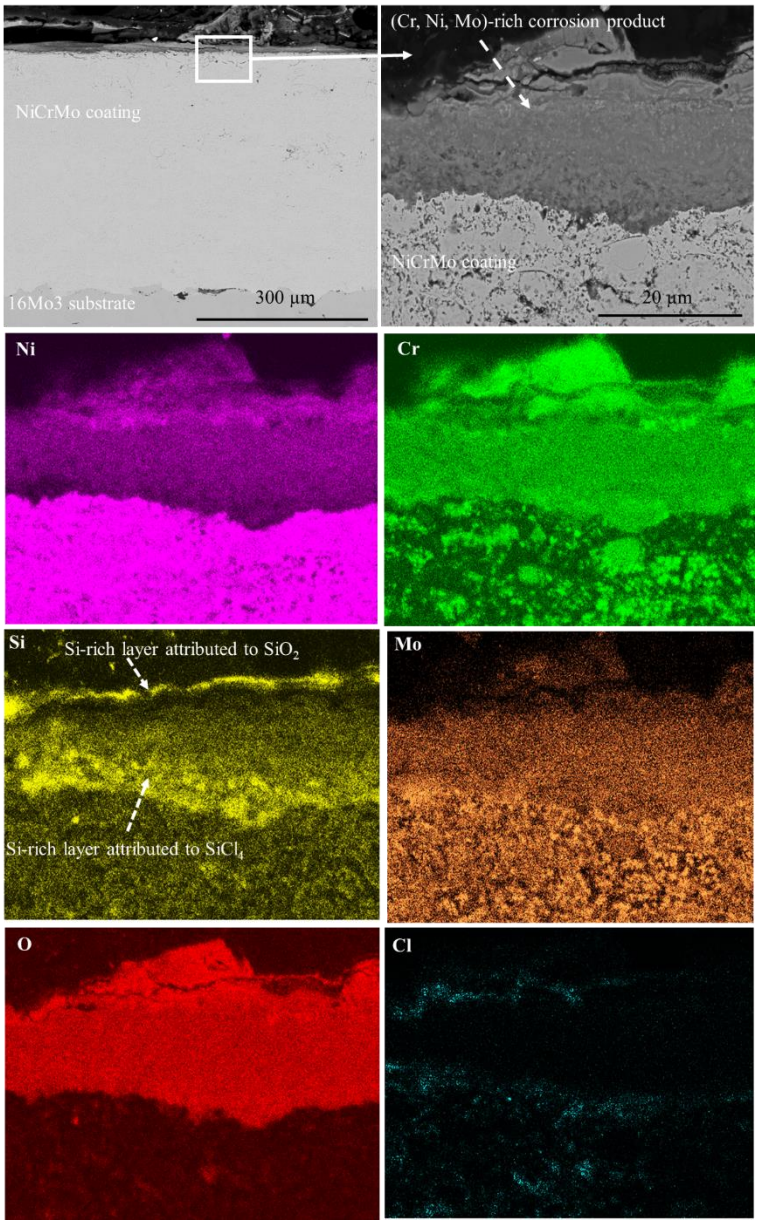

Fig. 10. Cross-sectional SEM micrograph (BSE) and EDS elemental mapping analysis of the NiCrMo coating oxidized in 5%O_2 + 500ppm HCl + N_2 with KCl deposit for 168 h at 600 °C.

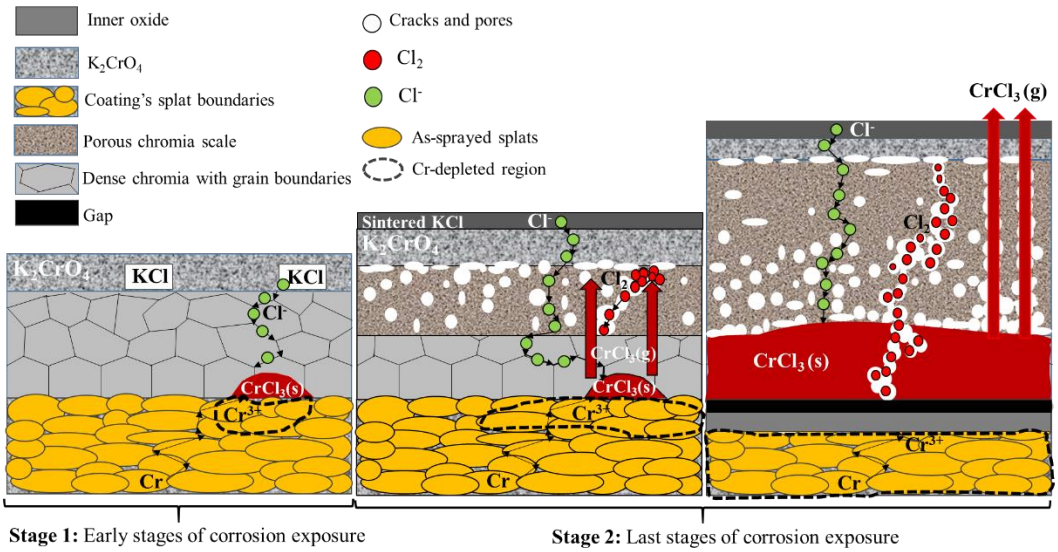

Fig. 11. Schematic of the proposed corrosion mechanisms in the coatings exposed to 5%O_2 + 500ppm HCl + N_2 with KCl for 168 h at 600 °C.